Int J Adv Manuf Technol (2016) 85:1915–1926
DOI 10.1007/s00170-016-8595-3

ORIGINAL ARTICLE

Numerical and experimental investigation on thermo-mechanical behavior during transient extrusion process of high-strength 7×××aluminum alloy profile

Cunsheng Zhang[1] · Shan Yang[1] · Cuixue Wang[1] · Guoqun Zhao[1] · Anjiang Gao[2] · Lanjun Wang[2]

Received: 22 October 2015 / Accepted: 2 March 2016 / Published online: 18 March 2016

Abstract Aluminum profile extrusion involves complex thermal, tribological, and mechanical interactions; thus, material flow and thermal behavior during extrusion process are very complicated. In this work, the material flow and thermal behavior of a 7×××aluminum alloy profile during an entire extrusion cycle are investigated numerically and experimentally. Hot compression tests are firstly carried out, and inverse analysis method is used to identify the material parameters of AA7N01 in Arrhenius constitutive model. The calculated global error is only 6.2 % between the predicted and experimental force–displacement curves, which verifies that the proposed model and obtained material parameters can describe well the rheological behavior of this alloy at elevated temperatures. Then a thermo-mechanical finite element model based on DEFROM-3D is built, and the transient extrusion process of the profile is simulated. By numerically analyzing the nose-end shape of the extruded profile, the evolution curves of exit temperature and of extrusion load, material flow and thermal behavior during extrusion process are investigated, respectively. Practical extrusion experiments verify the numerical model and results. Additional microstructure examination with electron backscatter diffraction (EBSD) technique also shows fine grains with the uniform grain size of about 9 μm on different locations of the extruded profile. Therefore, the material constitutive model and numerical model of extrusion process built in this work are capable enough to provide theoretical guidance in optimizing process parameters and designing extrusion dies.

Keywords Thermo-mechanical behavior · Transient extrusion process · Arrhenius constitutive model · Inverse analysis method · High-strength 7×××aluminum alloy

✉ Guoqun Zhao
zhaogq@sdu.edu.cn; zhangcs@sdu.edu.cn

[1] Key Laboratory for Liquid-Solid Structural Evolution & Processing of Materials (Ministry of Education), Shandong University, Jinan, Shandong 250061, People's Republic of China

[2] Conglin Aluminum Co., Ltd., Yantai, Shandong 265705, People's Republic of China

1 Introduction

Aluminum alloy profiles are widely used in building, rail transportation, aerospace, large engineering structures, communications, and other fields thanks to their low density, high specific strength, good appearance, good corrosion resistance, easy recycling, etc. As a typical three-dimensional, nonlinear, and large deformation process, aluminum profile extrusion involves complex thermal, tribological, and mechanical interactions; thus, material flow and thermal behavior during extrusion process are very complicated. The more developed numerical simulation method has been proven to be an efficient tool to understand deeply the material deformation behavior and to provide theoretical guidances for determining extrusion process parameters and designing extrusion dies.

Due to severe mesh distortion, frequent re-meshing, and low simulation efficiency, many researchers investigated the steady-state extrusion stage by ignoring transient effects during the extrusion process. Gouveia et al. [1, 2] simulated the steady-state stages of two- and three-dimensional forward extrusions by both the updated Lagrangian and the combined Eulerian–Lagrangian finite element formulations. It was found that the latter formulation was greatly advantageous in reducing the computation time, overcoming the frequent re-meshing, and predicting more accurately. He et al. [3] used HyperXtrude to simulate the steady extrusion process for a

complicated aluminum alloy profile. The nose-end shape of the extruded profile by numerical simulation was basically consistent with the experimental one. Chen et al. [4] investigated the effects of eccentricity ratio, shape of the second-step welding chamber, and uneven bearing length on the exit velocity distribution of extrudate by simulating a multi-hole extrusion process of a hollow and thin wall aluminum profile and designed a two-hole porthole die accordingly. The uniform exit velocity and temperature distribution on the extrudate with the optimized die were obtained. Liu et al. [5] simulated the steady-state extrusion process of a large, multi-cavity aluminum profile for high-speed train, and the numerical results agreed well with the experimental ones. By resizing portholes, adding baffle plates, chamfering mandrels, and adjusting the length of the bearings, an optimized die with uniform exit velocity was designed. Zhang et al. [6–8] analyzed the effects of extrusion process parameters (such as stem speed) and die structures (such as baffle plate, die orifice layout) on extrusion process, such as metal flow behavior at die exit, temperature distribution, extrusion force, welding pressure, etc. And they investigated the effects of process parameters on the metal flow uniformity and on the extrusion force with Taguchi's design of experiment. Through analysis, the optimum combinations of process parameters for uniform flow velocity distribution and minimum extrusion force were obtained [9].

However, at the beginning stage of an extrusion process, metal impacts extrusion die bridges instantaneously and sharply, which causes easily extrusion die's damage. While at the final stage, the back-end defects often occur due to the radial flow of material. As a result, it is very necessary to carry out the transient simulation of an entire extrusion cycle.

Jo et al. [10–12] simulated porthole die extrusion process in the non-steady state to analyze the material flow behavior and to determine the welding pressure of hot extrusion products by changing extrusion ratio, billet temperature, bearing length, and tube thickness. Li et al. [13] investigated numerically and experimentally the effect of inner cone punch on the mechanical mechanisms of metal flow behavior in the extrusion process. Hwang et al. [14] analyzed the metal flow of an inner billet covered with an outer oxidation layer during rod extrusion and studied the influence of various extrusion conditions on the critical ram stroke length and on the length of the product with surface permeation defects based on DEFORM-2D and experiments. Bingöl et al. [15] combined DEFORM-3D with artificial neural network to study the effects of extrusion parameters on the extrusion load of gear-like profile extrusion with experiment verification. Chanda et al. [16, 17], Zhou et al. [18], and Li et al. [19, 20] studied the influence of ram speed on the exit temperature uniformity along the extrusion direction and obtained the appropriate ram speeds, which was verified experimentally. Zhang et al. [21] investigated the effects of process parameters (stem speed, extrusion temperature, friction coefficient, etc.) on the wear behavior of a porthole extrusion die by implanting the modified Archard's model into DEFORM-3D, and it was shown that a minimum wear depth occurred at a certain temperature in the range of 400–425 °C. Halvorsen et al. [22] studied the mechanisms of buckling and waving of an extruded strip based on Msc SuperForm software. Extrusion experiments were performed in order to verify both numerical results and the mechanisms observed in the FEM simulations. Wu et al. [23] simulated the extrusion process of an aluminum rectangular hollow pipe based on Msc/SuperForge. They proposed three die modification schemes and determined the optimal one. Hatzenbichler et al. [24] performed a numerical sensitivity study with DEFORM-2D to determine the main influencing parameters on the length of the back-end defect during extrusion process. It was found that friction and geometric process parameters influenced significantly the back-end defect. Fang et al. [25–27] studied the effects of pocket shape, number of pocket steps, bearing length, and ram speed on the material flow of extrusion process. Bastani et al. [28, 29] utilized ALMA2π and HyperXtrude to investigate the effects of process parameters including front billet temperature, billet temperature taper, ram speed, and container cooling on the exit velocity and temperature uniformity along the radial and axial directions. Peng et al. [30] studied the influence of the number and the distribution of die holes on the extrusion parameters with Forge3D. They also studied the influence of the pocket on exit velocity, temperature, and deformation field distributions in multi-hole extrusion and obtained an appropriate pocket structure [31].

As one of the typical Al-Zn-Mg series aluminum alloys developed by Japan, AA7N01 has high strength and good extrusion performance and welding performance [32], so it has been widely used in the components requiring high fracture toughness as well as high strength, such as cross beams, traction beams, and sleeper beams used in high-speed train. However, most works in the literature regarding AA7N01 focus on the chemical composition design, aging system, and their influences on mechanical properties, there exists little investigation on the material flow and thermal behavior during extrusion process.

Therefore, the purpose of this work is to numerically and experimentally investigate the thermo-mechanical behavior of an AA7N01 beam profile used in high-speed train. Firstly, the constitutive model of AA7N01 will be determined by the inverse analysis method based on hot compression tests. Then, a thermo-mechanical finite element model based on DEFORM-3D will be built to investigate material flow and thermal behavior during an entire extrusion cycle. Finally, by comparing with the practical extrusion experiment, the material constitutive model and numerical model will be verified.

Table 1 Chemical composition of the as-received 7N01 aluminum alloy

Element	Si	Fe	Cu	Mn	Mg	Cr	Zn	Ti	Al
(w%)	<0.30	<0.35	0.20	0.15	1.80	0.20	5.0	0.10	Bal.

2 Experimental material and hot compression tests

To accurately describe the high-temperature deformation behavior of AA7N01, hot compression tests are carried out under different temperatures (350, 400, 450, 500, and 550 °C) and different strain rates (0.01, 0.1, 1.0, and 10/s). And then material parameters in constitutive model of AA7N01 are determined with inverse analysis method.

2.1 Experimental material

Based on our previous work, AA7N01 with the following chemical composition (Table 1) is chosen for experimental material in the present work.

The AA7N01 ingot is cast by the hot-top level pour casting method and then homogenized to eliminate casting stress, composition, and grain size segregation. The homogenization process curve is shown in Fig. 1. The ingots are firstly heated to the homogenization temperature of 450 °C at the heating rate of 80 °C/h, and held for 12 h, then heated to 465 °C and held for 5 h during the second homogenizing stage, then cooled 2 h in the air, after that, 0.5 h in the water to 60~80 °C, and finally cooled in the air to room temperature. The microstructure of AA7N01 ingot after homogenizing processing is shown in Fig. 2, where the uniform grain structure is observed.

2.2 Hot compression tests

The cylindrical specimens with a diameter of 10 mm and a height of 15 mm are machined from the homogenized ingot.

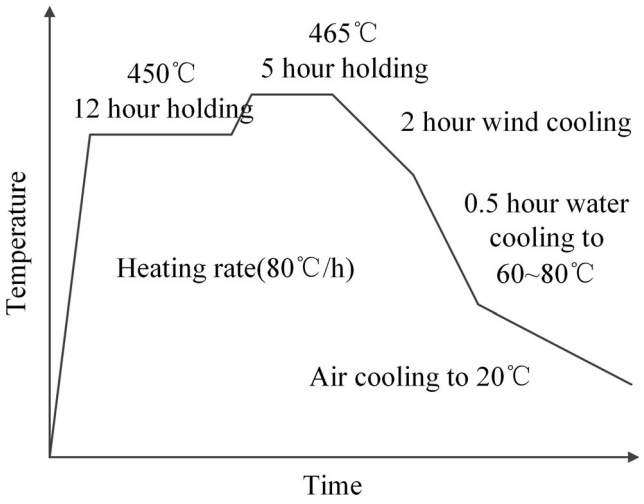

Fig. 1 Temperature controlling curve for homogenization

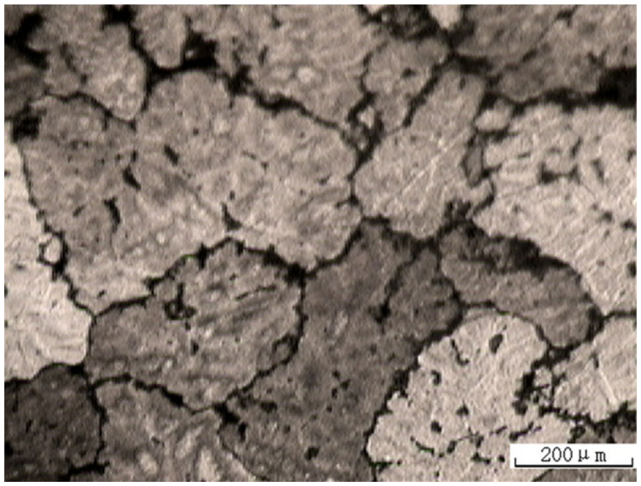

Fig. 2 Micro-structure of billet after homogenization

Before the experiments, graphite foils are used as lubricant to minimize the friction between the specimens and tool head. The experimental parameters of hot compression tests are as follows: the test temperatures of 350, 400, 450, 500, and 550 °C, the strain rates of 0.01, 0.1, 1.0, and 10/s, and the total deformation extent of 50 %. Before the compression tests, the specimens are heated to the deformation temperature and held for 2 min, then compressed at a constant strain rate, and finally quenched with water immediately at the end of the compression tests. The temperature curve during the compression test is shown in Fig. 3.

The measured true stress–strain curves at temperatures ranging from 350 to 550 °C and strain rates from 0.01 to 10/s are smoothed and presented in Fig. 4. It can be found that the effects of the temperature and strain rate on the flow stress are significant. The flow stress decreases with the increasing temperature and the decreasing strain rate. At the early deformation stage, the flow stress increases rapidly with the increase of strain, which results from the work hardening caused by the dislocation generation and multiplication [33]. After a rapid increase, the flow stress begins to increase slowly until the

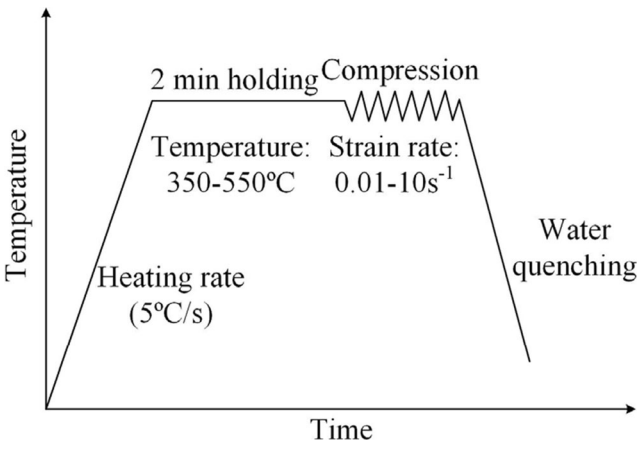

Fig. 3 Temperature controlling curve during compression tests

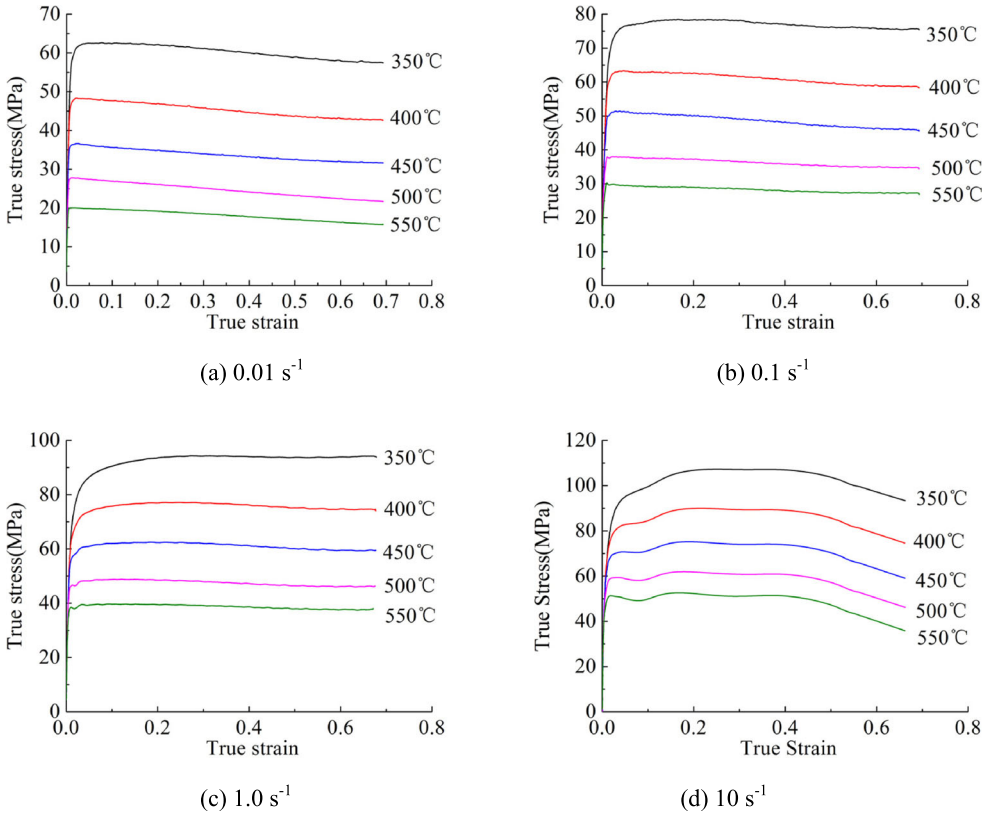

Fig. 4 True stress-strain curves of AA7N01 obtained at different temperatures under (**a**) 0.01 s^{-1}, (**b**) 0.1 s^{-1}, (**c**) 1.0 s^{-1} and (**d**) 10 s^{-1}

maximum flow stress is reached. Then, the flow stress tends to decline or maintain a steady state, illustrating a dynamic equilibrium between the work hardening and dynamic softening [34]. When the strain rate is 10/s (Fig. 4d), the true stress–strain curves show more vibrations than those with low strain rates, which can be explained by the periodic repetition of material softening and hardening [35].

3 Identification of material parameters by inverse analysis method

The material parameters in constitutive models are commonly determined by the traditional linear fitting method [36–39]. Thus, the influence of the inhomogeneous deformation and the plastic deformation heat during the hot compression test cannot be taken into account when calculating material parameters, which leads to low computational accuracy and efficiency. Therefore, the inverse analysis method is used to identify material parameters in this work. Based on the numerical simulation and experimental data, the inverse analysis is to minimize the difference between the calculated values and the corresponding experimental data by adjusting the unknown material parameters according to the selected optimization algorithm [40–43]. This method compares directly the forces and displacements obtained numerically and experimentally, which could effectively avoid the error caused in the calculation of stresses and strains.

3.1 Arrhenius constitutive model

The Arrhenius constitutive model is applied in this paper to describe the hot deformation behavior of 7N01:

$$\sigma = \frac{1}{\alpha}\sin^{-1}\left[\left(\frac{Z}{A}\right)^{\frac{1}{n}}\right] \tag{1}$$

where σ is the flow stress (MPa); α, n, and A are the temperature-independent material parameters; and Z is the Zener–Hollomon parameter (/s), defined by:

$$Z = \dot{\varepsilon}\exp\left(Q\Big/RT\right) \tag{2}$$

where $\dot{\varepsilon}$ is the train rate (/s), Q is the activation energy (J/mol), R is the universal gas constant (8.314 J/(mol · K)), and T is the absolute temperature (K). In Eqs. 1 and 2, α, n, A, and Q are unknown material parameters to be identified.

3.2 Integration of Arrhenius constitutive model into ABAQUS

To simulate the hot compression tests with ABAQUS software, Arrhenius constitutive model is embedded by UHARD

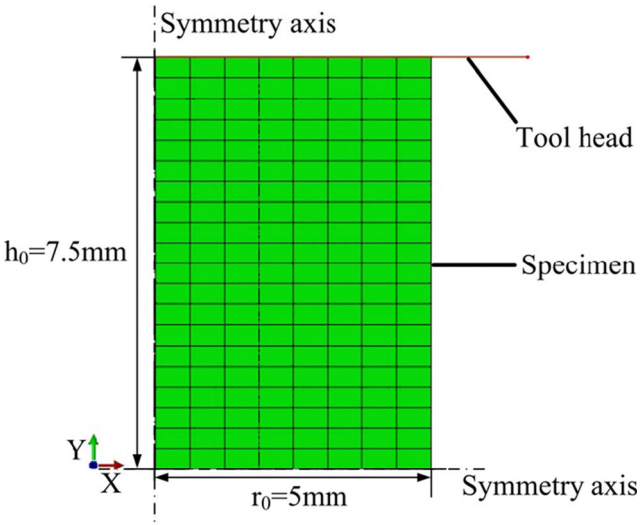

Fig. 5 FE model used for the inverse analysis

subroutine. Four variables, including SYIELD, HARD(1), HARD(2), HARD(3), need to be self-defined in the UHARD subroutine, where SYIELD is yield stress for isotropic plasticity; HARD(1), HARD(2), and HARD(3) are the variations of SYIELD with respect to the plastic strain, the plastic strain rate, and temperature, respectively. The following expressions should be coded in UHARD subroutine.

$$SYIELD = \sigma\left(\varepsilon, \dot{\varepsilon}, T\right) = \frac{1}{\alpha}\sinh^{-1}\left(\frac{Z}{A}\right)^{\frac{1}{n}} \tag{3}$$

$$HARD(1) = \partial\sigma\left(\varepsilon, \dot{\varepsilon}, T\right)\Big/\partial\varepsilon = 0 \tag{4}$$

$$HARD(2) = \partial\sigma\left(\varepsilon, \dot{\varepsilon}, T\right)\Big/\partial\dot{\varepsilon} = \left(\frac{Z}{A}\right)^{\frac{1}{n}}\Big/\left(\dot{\varepsilon}\left(\left(\frac{Z}{A}\right)^{\frac{2}{n}}+1\right)^{\frac{1}{2}}\alpha n\right) \tag{5}$$

$$HARD(3) = \partial\sigma\left(\varepsilon, \dot{\varepsilon}, T\right)\Big/\partial T = -\left(\frac{Z}{A}\right)^{\frac{1}{n}}Q\Big/\left(RT^2\left(\left(\frac{Z}{A}\right)^{\frac{2}{n}}+1\right)^{\frac{2}{n}}\alpha n\right) \tag{6}$$

3.3 Construction of FEM model in ABAQUS

Considering the symmetry of the FE model, a 2D axi-symmetric model is adopted in the numerical simulation to improve computational efficiency. The height of the model is half the physical specimen and the rigid tool head is simplified as a straight line, as shown in Fig. 5. During hot compression tests, part of the work generated by plastic deformation is

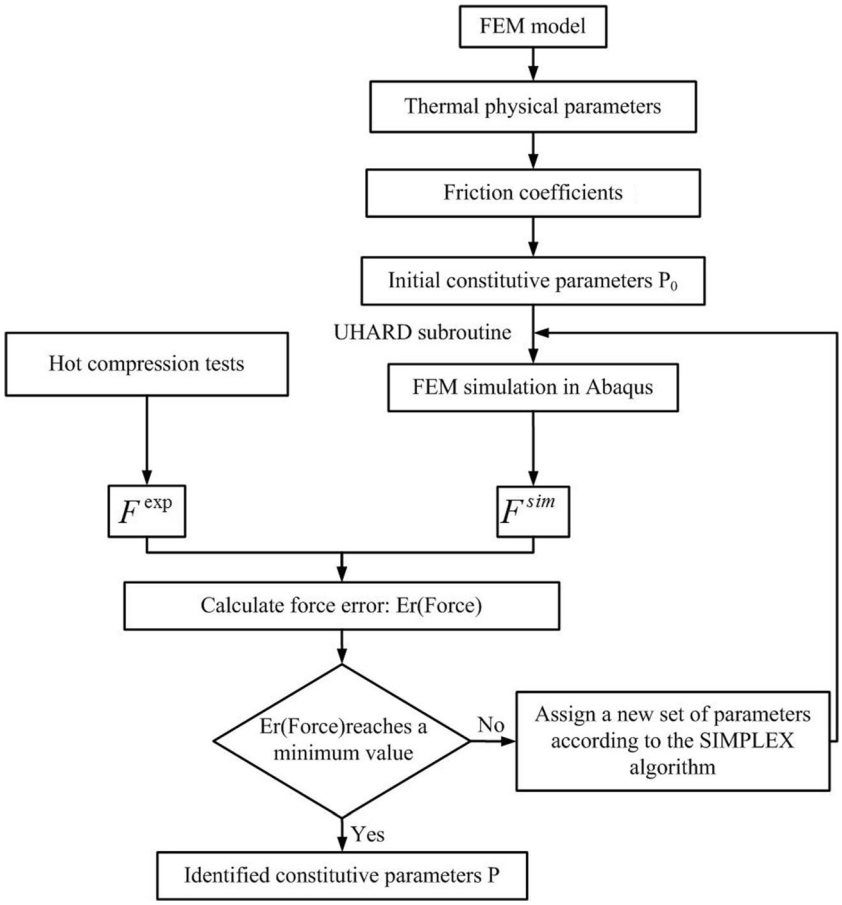

Fig. 6 Flow chart of the inverse analysis method in this work

Table 2 Material parameters of AA7N01 obtained by inverse analysis method

α (1/MPa)	Q (J/mol)	A (1/s)	Number
2.351E−002	2.041E+005	3.994E+012	5.752

transformed into heat, leading to the temperature increase and the change of the required force. Therefore, a thermal-coupled finite element model is developed in this work, in which the heat transformation is considered by defining the specific heat, the thermal conductivity, the density, and the inelastic heat fraction. Identical forming temperatures (350, 400, 450, 500, and 550 °C) and strain rates (0.01, 0.1, 1.0, and 10/s) are specified in the FE model to simulate the experimental compression tests. The stroke of the tool head is 3.75 mm.

3.4 Identification of material parameters

In this work, the optimization algorithm, the FEM simulation, and the error calculation are integrated by means of the optimization software modeFRONTIER. The minimization of the error between the experimental and predicted forces is set as the optimization objective, then four unknown material parameters of the constitutive model are identified by the inverse analysis. The flow chart of the inverse analysis technique is shown in Fig. 6.

1) Construct the FEM model of hot compression test based on ABAQUS. Define the thermal physical parameters of AA7N01 and friction coefficients. According to our previous work on 6 × × × aluminum alloy [43], strain rate and forming temperature have little effects on friction coefficients, whose values are close to 0.1 under all experimental conditions. Therefore, the friction coefficients between specimens and tool head for all experimental conditions in this work are defined as a same value of 0.1.
2) Define material parameters in UHARD subroutine as the unknown variables to be identified and meanwhile assign the initial values (P_0).
3) Run ABAQUS and launch UHARD subroutine to simulate hot compression tests and output forces and displacements according to the defined time interval.
4) Use the least square method to calculate the relative error between experimental and numerical forces at different displacement points. The expression is as follows:

$$E_r(\text{force}) = \frac{\sum_{i=0}^{N}\left[F_i^{\exp} - F_i^{\text{sim}}\right]^2}{\sum_{i=0}^{N}\left[F_i^{\exp}\right]^2} \tag{7}$$

where $F_i^{\exp}$ and F_i^{sim} denotes the forces obtained by experiments and FE simulation at the ith displacement point, respectively. N is the number of displacement points.
5) Check whether the error has reached a minimum value and shows a stable distribution. If it is true, the assigned constitutive parameters at current iteration step are the final optimum values. Otherwise, reassign a new set of material parameters according to the optimization algorithm and return to continue a new iteration process. Finally, the identified material parameters can be obtained (P).

3.5 Comparison between experimental and predicted force–displacement curves

The identified material parameters of AA7N01 are given in Table 2. The measured force–displacement curves and the predicted ones by the inverse analysis method under different strain rates at 350 and 400 °C are showed in Fig. 7 as examples. By comparison, it can be seen that the predicted curves show relatively good agreement with the experimental ones. The calculated global error is only 6.2 % indicating that the constitutive model obtained can well describe the deformation behavior of AA7N01. In the subsequent work, the constitutive

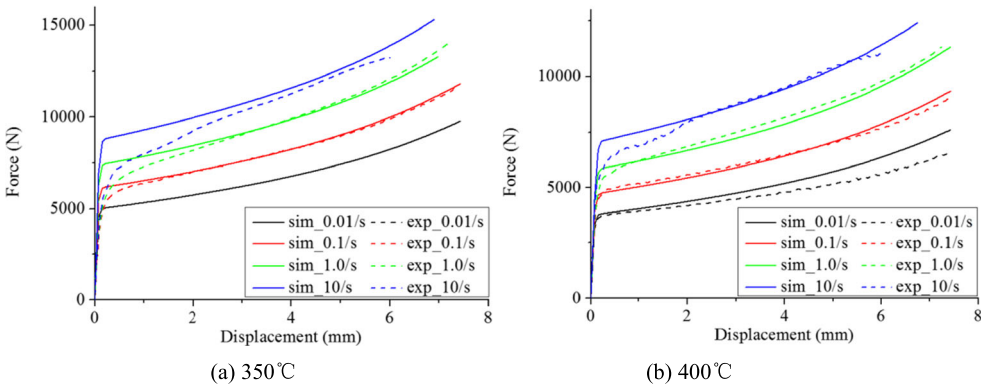

(a) 350℃ (b) 400℃

Fig. 7 Comparison between experimental and predicted force-displacement curves at (**a**) 350 °C and (**b**) 400 °C

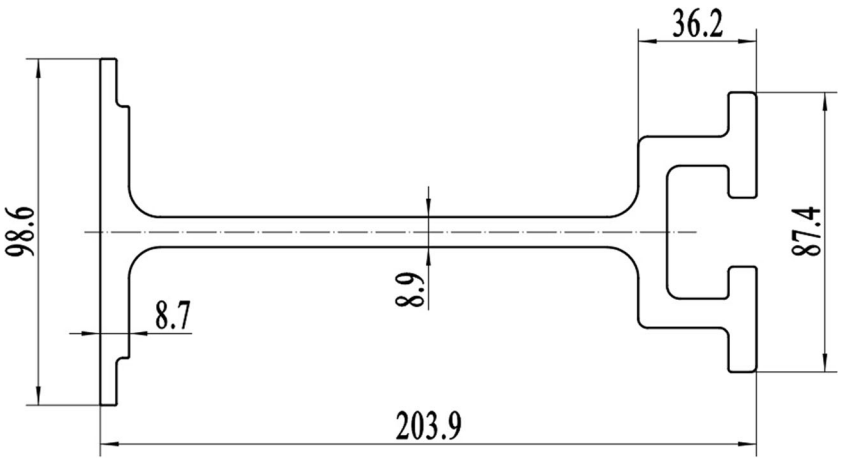

Fig. 8 Cross-section shape of the profile in this work (unit: mm)

model will be embedded into DEFORM-3D to simulate the transient extrusion process of AA7N01 profile.

4 Construction of FEM model of extrusion process of AA7N01 profile

4.1 Geometry feature of the profile and die design

The cross-section shape of the profile studied in this work is shown in Fig. 8. The maximum and minimum wall thicknesses are 18.2 and 4.3 mm, respectively. Though it is a solid profile, the large difference in wall thickness may lead to the difficulty in controlling size and shape of the profile. Especially 7N01 is a high strength and hard aluminum alloy with relatively poor plasticity compared to 6×××aluminum alloys, so it is difficult to extrude and to design extrusion dies too. Figure 9 shows the 2D geometry of the extrusion die specially designed according to the geometry feature and material characteristics. In order to better balance material flow in die cavity, a dumbbell-shaped pocket structure and die bearing with unequal lengths are used. Thanks to the symmetry of the whole model, only half model is used in FE simulation to reduce the total computing time, as shown in Fig. 10.

4.2 Definition of extrusion process parameters

AA7N01 and H13 are assigned for the billet and the tooling (die, container, and ram), respectively. As a more dedicated aluminum alloy, there is no material data of AA7N01 in

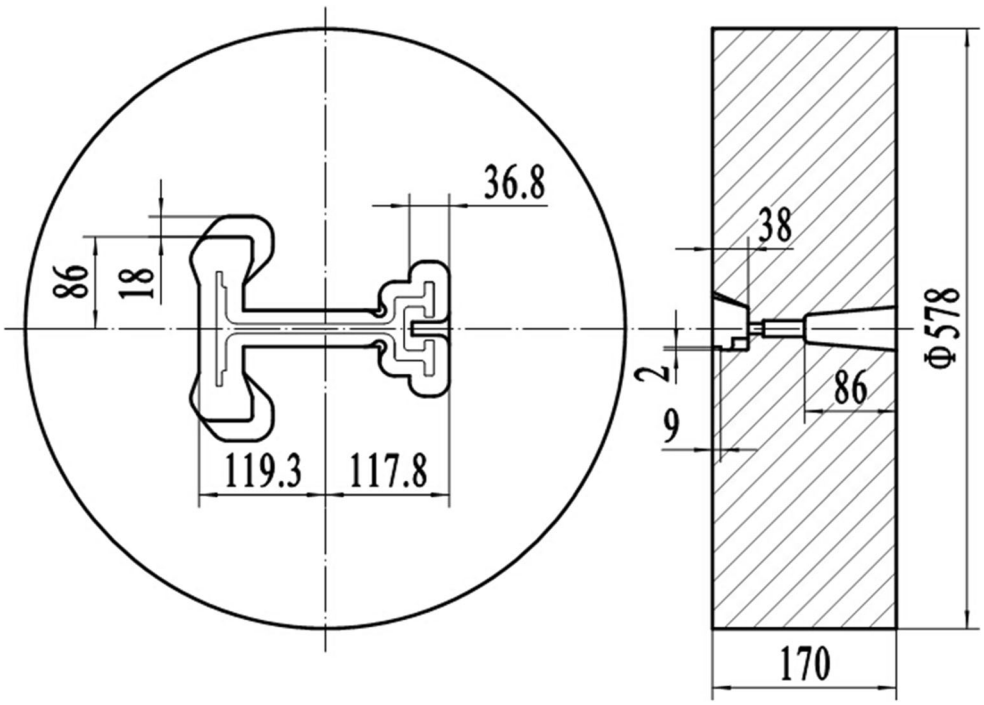

Fig. 9 2D geometry of the extrusion die (unit: mm)

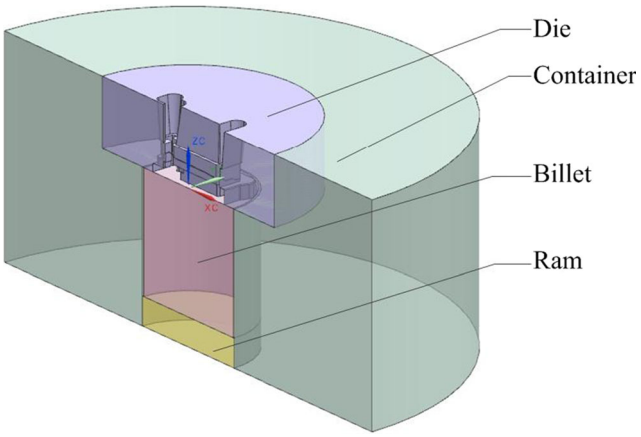

Fig. 10 Schematic drawing of the extrusion assembly

DEFORM's material library, so the above constitutive equation is embedded into DEFORM-3D to describe the material behavior during extrusion process. The extrusion process parameters used in the simulation are listed in Table 3. The heat transfer coefficient between the billet and the extrusion tooling is 11 N/s/mm/. The friction type between aluminum and the bearing is coulomb friction with the friction coefficient of 0.3, while the shear friction is assigned between aluminum and the other tooling surfaces with the friction coefficient of 0.8.

4.3 Material flow and thermal behavior analysis during transient extrusion process

In order to verify the numerical model and compare with numerical results, the extrusion experiment is carried out on 44 MN extrusion press. It should be pointed out that the billet length in the practical production is 850 mm, while that in the simulation is chosen as 300 mm to reduce the computing time. The only difference is the duration of the steady stage between numerical simulation and experiment. The extrusion die assembly and the extruded profile are given in Figs. 11 and 12, respectively.

4.4 Nose-end shapes of the extruded profile

The nose-end shape of the extruded profile is used to repair the extrusion die and control the size and shape of a profile. The comparison of nose-end shapes of the extruded profile from numerical simulation and experiment is given in Fig. 13. It is clear that the material flows a little faster at the T junctions of the profile than that in other areas. But in general, the material flows across the whole cross-section are relatively uniform, and thus the deformation of the profile is very small. What is more, it can be seen that the shape of the nose end of the profile by FE simulation shows excellent agreement with experimental observation, which indicates that the FE model could well predict the material flow behavior during the extrusion process.

Table 3 Extrusion process parameters in the FE simulation

Billet diameter (mm)	312
Billet length (mm)	300
Container diameter (mm)	320
Extrusion ratio	19.2
Billet temperature (°C)	490
Die temperature (°C)	480
Container temperature (°C)	440
Extrusion stem temperature (°C)	490
Ram velocity (mm/s)	1.5

Fig. 11 Extrusion die assembly used in experiment

The exit velocity distribution of the extruded profile is shown in Fig. 14. It can be seen that the maximum velocity is 46 mm/s at the T junctions and the minimum velocity is 39 mm/s at the tips. The small difference in material flow velocity of 7 mm/s does not cause the distortion deformation during extrusion process.

4.5 Evolution curve of exit temperature on the profile

The exit temperature has a critical effect on mechanical properties and microstructure of the profile. A non-contact

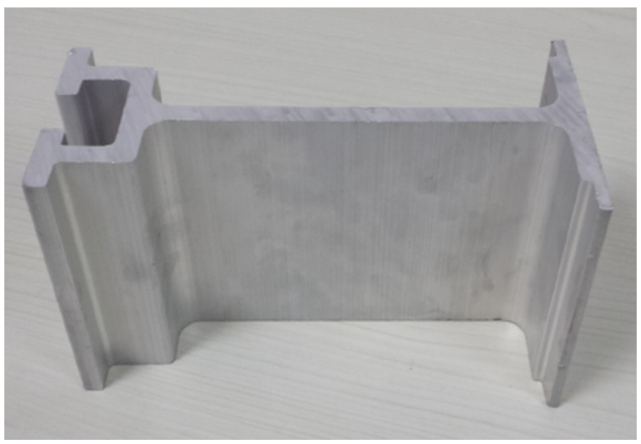

Fig. 12 Extruded profile in experiment

Fig. 13 Nose-ends of the extruded profile from (**a**) experiments and (**b**) FE simulation

infrared thermometer is used in experiment to detect the temperature of the extruded profile at the press exit. The temperature evolution curves on the profile at the press exit during the entire extrusion process by experiments and FE simulation are showed in Fig. 15. Taking into accout the non-uniform speed of extrusion ram during the practical extrusion process, there does not exist the completely proportional relationship between the time and ingot length, which is different from that in the numerical simulation.

At the initial filling stage, the billet is upsetted in the container and formed severely at die bearing; as a result, the largely generated heat leads to the increase of the temperature of the extruded profile. As the extrusion proceeds, the extrusion process tends to a steady stage, and the exit temperature of the extruded profile remains substantially stable. In the finally turbulent stage, material flows sharply from the surrounding to the center perpendicular to the extrusion direction, leading again to the increase of the exit temperature of the extruded profile. By comparison, it can be seen that the evolution curve of exit temperature by FE simulation is consistent with experiment one. And the average exit temperature on the extruded profile is about 513 °C in the steady-state stage, which is appropriate for qualified product without microstructure defects, such as coarse grains, overheating, or even overburning.

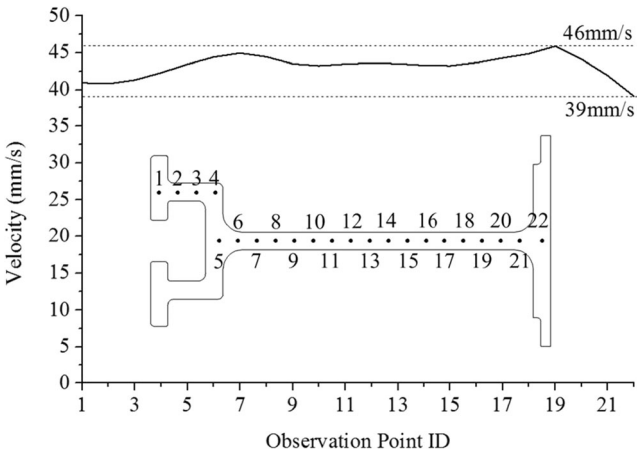

Fig. 14 Exit velocity distribution of the extruded profile

4.6 Extrusion load analysis

The obtained extrusion load curves from experiment and FE simulation are given in Fig. 16, which can be clearly divided into three stages. At the beginning stage (stage I), the material gradually fills the container and the pocket under the pressure of ram. The extrusion load increases up to maximum value, which is called the breakthrough extrusion load. At the steady stage (stage II), the extrusion load declines with the decreasing billet length. At the final stage (stage III), the extrusion load slightly increases again due to the turbulent flow of the material. By comparison, it can be seen that the breakthrough extrusion load in the experiment is 36 MN, while it is 39 MN by numerical simulation.

From above analysis, the nose-end shapes of the extruded profile, the evolution curves of exit temperature, and of extrusion load obtained from simulation and experiment show excellent agreements. Accordingly, the material constitutive equation and numerical model of extrusion process built in this work are both well verified, which could be used to provide theoretical guidance in optimizing process parameters and designing extrusion dies.

4.7 Microstructure observations of the extruded profile

Four different points on the extruded profile are chosen to observe their microstructures, as shown in Fig. 17. The

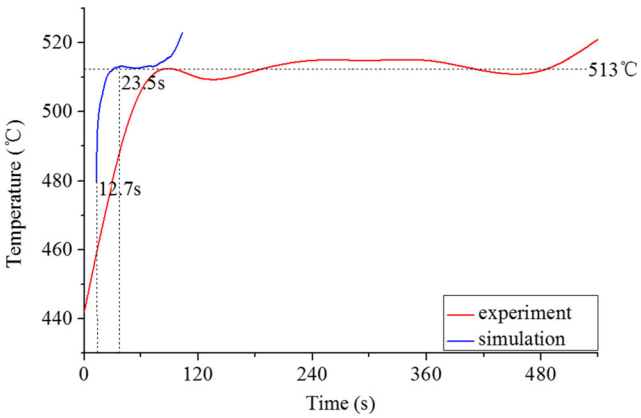

Fig. 15 Temperature evolution curves of the extruded profile at the press exit

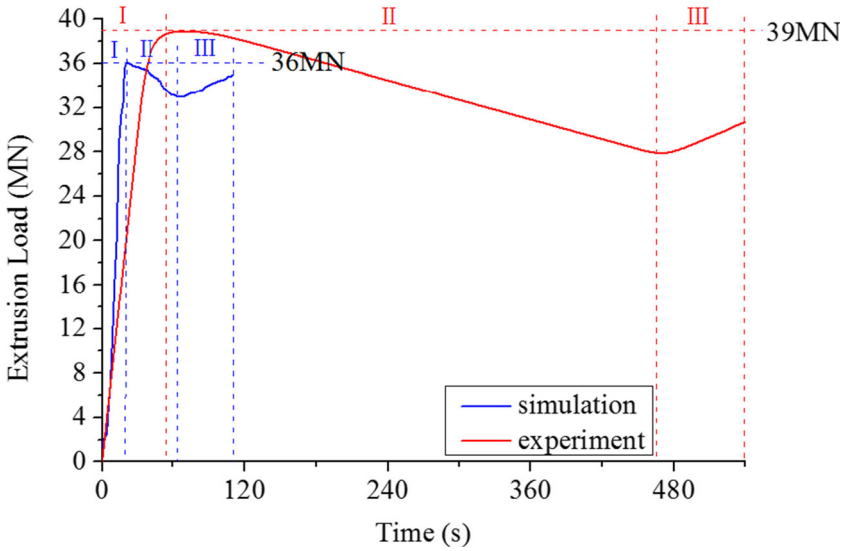

Fig. 16 Extrusion load curves obtained with experiment and simulation

recrystallized grain boundaries cannot be resolved using optical microscopy, and therefore electron backscatter diffraction (EBSD) technique is used in this work. Figure 18 shows the grain size and distribution on different observation points by EBSD technique. As can be seen from the figure, there are a lot of equi-axed recrystallized grains and some equi-axed recrystallization nuclei occur at the grain boundaries. The deformation organization has basically disappeared. Due to the uniform velocity and temperature distributions in the cross-section of the profile, the grain size in different zones of the profile has a similar value of about 9 μm, which shows that the profile with uniform mechanical property has been obtained in this work.

5 Conclusions

In this work, inverse analysis method was used to identify material parameters in Arrhenius constitutive model for the numerical simulation of the extrusion process of AA7N01 profile. By numerical results and experimental extrusion observations, the thermo-mechanical behavior during an entire extrusion cycle was investigated. The main conclusions were drawn as follows:

1) Based on the combination of hot compression tests, ABAQUS, and modeFRONTIER, the material parameters in Arrhenius constitutive model of AA7N01 were identified by inverse analysis method. Taking into account the influence of the inhomogeneous deformation and plastic deformation heat during the hot compression test, the inverse analysis method improved greatly the computational accuracy. The predicted force–displacement curves showed good agreement with the experimental ones under different temperatures and strain rates. The calculated global error was only 6.2 % indicating that the constitutive model and its material parameters could well describe the deformation behavior of AA7N01 at elevated temperature.
2) With the identified material parameters, the transient extrusion simulation of an AA7N01 profile was carried out to investigate the material flow and thermal behavior. The

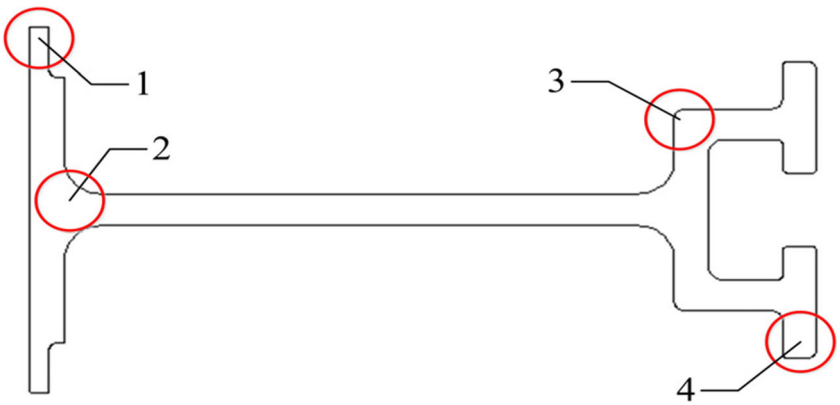

Fig. 17 Distribution of the observation points on the cross-section of the profile

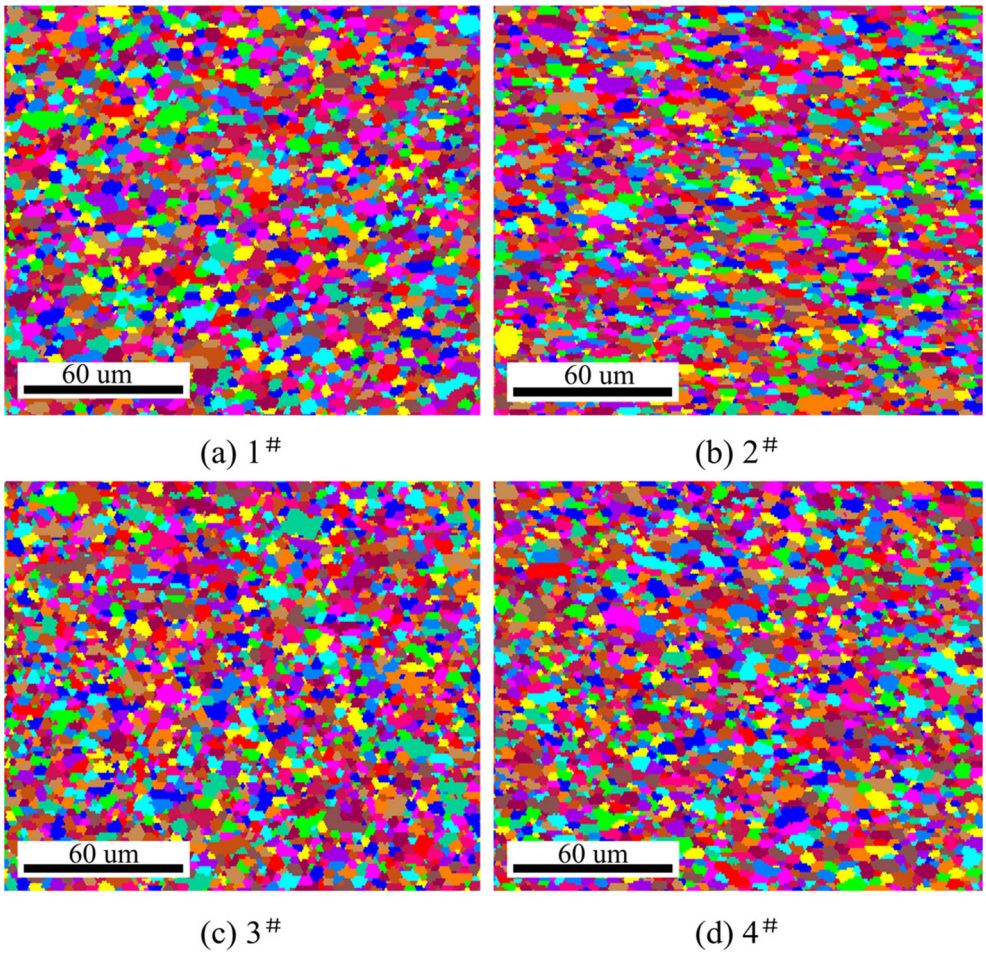

Fig. 18 Micro-structures in different observation points of (**a**) 1#, (**b**) 2#, (**c**) 3# and (**d**) 4# on the profile with EBSD

practical extrusion process was also realized in the workshop. The nose-end shapes of the extruded profile and the evolution curves of exit temperature and of extrusion load obtained from simulations and experiment showed excellent agreements, except that the breakthrough extrusion load of 36 MN by numerical simulation was lower than 39 MN in experimental observation.

Acknowledgments The authors would like to acknowledge the financial support from the National Natural Science Foundation of China (51575315 and 51375270) and the Fundamental Research Funds of Shandong University (2015WLJH29 and 2015JC046).

References

1. Gouveia BPPA, Rodrigues JMC, Bay N, Martins PAF (1999) Finite-element modelling of cold forward extrusion. J Mater Process Technol 94:85–93
2. Gouveia BPPA, Rodrigues JMC, Bay N, Martins PAF (2000) Deformation analysis of the round-to-square extrusion: a numerical and experimental investigation. Finite Elem Anal Des 35:269–282
3. He Z, Wang HN, Wang MJ, Li GY (2012) Simulation of extrusion process of complicated aluminium profile and die trial. Trans Nonferrous Met Soc Chi 22:1732–1737
4. Chen L, Zhao GQ, Yu JQ, Zhang WD, Wu T (2014) Analysis and porthole die design for a multi-hole extrusion process of a hollow, thin-walled aluminum profile. Int J Adv Manuf Technol 74:383–392
5. Liu P, Xie SS, Cheng L (2012) Die structure optimization for a large, multi-cavity aluminum profile using numerical simulation and experiments. Mater Des 36:152–160
6. Zhang CS, Zhao GQ, Chen ZR, Chen H, Kou FJ (2012) Effect of extrusion stem speed on extrusion process for a hollow aluminum profile. Mater Sci Eng B 177:1691–1697
7. Zhang CS, Zhao GQ, Sun XM, Chen H, Gao BJ (2011) Optimization design of baffle plates in porthole die for aluminum profile extrusion. J Mater Des Appl 225(4):255–265
8. Zhang CS, Zhao GQ, Chen H, Guan YJ, Cai HJ, Gao BJ (2013) Investigation on effects of die orifice layout on three-hole porthole extrusion of aluminum alloy 6063 tubes. J Mater Eng Perform 22(5):1223–1232
9. Zhang CS, Zhao GQ, Chen H, Guan YJ, Li HK (2012) Optimization of an aluminum profile extrusion process based on Taguchi's method with S/N analysis. Int J Adv Manuf Technol 60: 589–599
10. Jo HH, Lee SK, Lee SB, Kim BM (2002) Prediction of welding pressure in the non-steady state porthole die extrusion of Al7003 tubes. Int J Mach Tool Manuf 22:753–759

11. Jo HH, Jeong CS, Lee SK, Kim BM (2003) Determination of welding pressure in the non-steady-state porthole die extrusion of improved Al7003 hollow section tubes. J Mater Process Technol 139:428–433
12. Jo HH, Lee SK, Jung CS, Kim BM (2006) A non-steady state FE analysis of Al tubes hot extrusion by a porthole die. J Mater Process Technol 173:223–231
13. Li F, Jin JF, Guan J, Liu XJ (2009) Effect of inner cone punch on metal flow in extrusion process. Int J Adv Manuf Technol 42:489–496
14. Hwang YM, Chen JM (2013) Surface permeation and die design during rod extrusion processes. Int J Adv Manuf Technol 69:397–403
15. Bingöl S, Ayer Ö, Altinbalik T (2015) Extrusion load prediction of gear-like profile for different die geometries using ANN and FEM with experimental verification. Int J Adv Manuf Technol 76:983–992
16. Chanda T, Zhou J, Kowalski L, Duszczyk J (1999) 3D FEM simulation of the thermal events during AA6061 aluminum extrusion. Scri Mater 41:195–202
17. Chanda T, Zhou J, Duszczyk J (2001) A comparative study on isospeed extrusion and isothermal extrusion of 6061 Al alloy using 3D FEM simulation. J Mater Process Technol 114:145–153
18. Zhou J, Li L, Duszczyk J (2004) Computer simulation and experimentally verified isothermal extrusion of 7075 aluminium through continuous ram speed variation. J Mater Process Technol 146:203–212
19. Li L, Zhou J, Duszczyk J (2004) Prediction of temperature evolution during the extrusion of 7075 aluminium alloy at various ram speeds by means of 3D FEM simulation. J Mater Process Technol 145:360–370
20. Li LX, Lou Y (2008) Ram speed profile design for isothermal extrusion of AZ31 magnesium alloy by using FEM simulation. Trans Nonferrous Met Soc Chi 18:s252–s256
21. Zhang CS, Zhao GQ, Li TT, Guan YJ, Chen H, Li P (2013) An investigation of die wear behavior during aluminum alloy 7075 tube extrusion. J Tribol-T ASME 135(1):011602-1-9
22. Halvorsen F, Aukrust T (2006) Studies of the mechanisms for buckling and waving in aluminum extrusion by use of a Lagrangian FEM software. Int J Plasticity 22:158–173
23. Wu XH, Zhao GQ, Luan YG, Ma XW (2006) Numerical simulation and die structure optimization of an aluminum rectangular hollow pipe extrusion process. Mater Sci Eng A 435–436:266–274
24. Hatzenbichler T, Buchmayr B, Umgeher A (2007) A numerical sensitivity study to determine the main influence parameters on the back-end defect. J Mater Process Technol 182:73–78
25. Fang G, Zhou J, Duszczyk J (2008) Effect of pocket design on metal flow through single-bearing extrusion dies to produce a thin-walled aluminium profile. J Mater Process Technol 199:91–101
26. Fang G, Zhou J, Duszczyk J (2009) FEM simulation of aluminium extrusion through two-hole multi-step pocket dies. J Mater Process Technol 209:1891–1900
27. Fang G, Zhou J, Duszczyk J (2009) Extrusion of 7075 aluminium alloy through double-pocket dies to manufacture a complex profile. J Mater Process Technol 209:3050–3059
28. Bastani AF, Aukrust T, Brandal S (2010) Study of isothermal extrusion of aluminum using finite element simulations. Int J Mater Form 3:367–370
29. Bastani AF, Aukrust T, Brandal S (2011) Optimisation of flow balance and isothermal extrusion of aluminium using finite-element simulations. J Mater Process Technol 211:650–667
30. Peng Z, Sheppard T (2004) Simulation of multi-hole die extrusion. Mater Sci Eng A 367:329–342
31. Peng Z, Sheppard T (2005) Effect of die pockets on multi-hole die extrusion. Mater Sci Eng A 407:89–97
32. J.I.S. Committee. Standard: JIS H4100-2006 Aluminium and aluminium alloy extruded shape, 2006.
33. Wen DX, Lin YC, Li HB, Chen XM, Jiao D, Li LT (2014) Hot deformation behavior and processing map of a typical Ni-based superalloy. Mater Sci Eng A 591:183–192
34. Li J, Li FG, Cai J, Wang RT, Yuan ZW, Xue FM (2012) Flow behavior modeling of the 7050 aluminum alloy at elevated temperatures considering the compensation of strain. Mater Des 42:369–377
35. Quan GZ, Li GS, Chen T, Wang YX, Zhang YW, Zhou J (2011) Dynamic recrystallization kinetics of 42CrMo steel during compression at different temperatures and strain rates. Mater Sci Eng A 528:4643–4651
36. Lin YC, Xia YC, Chen XM, Chen MS (2010) Constitutive descriptions for hot compressed 2124-T851 aluminum alloy over a wide range of temperature and strain rate. Comput Mater Sci 50:227–233
37. Haghdadi N, Zarei-Hanzaki A, Abedi HR (2012) The flow behavior modeling of cast A356 aluminum alloy at elevated temperatures considering the effect of strain. Mater Sci Eng A 535:252–257
38. Li J, Li F, Cai J, Wang RT, Yuan ZW, Ji GL (2013) Comparative investigation on the modified Zerilli–Armstrong model and Arrhenius-type model to predict the elevated-temperature flow behaviour of 7050 aluminium alloy. Comput Mater Sci 71:56–65
39. Chen L, Zhao GQ, Yu JQ, Zhang WD (2015) Constitutive analysis of homogenized 7005 aluminum alloy at evaluated temperature for extrusion process. Mater Des 66:129–136
40. Cho H, Altan T (2005) Determination of flow stress and interface friction at elevated temperatures by inverse analysis technique. J Mater Process Technol 170:64–70
41. Zhou JM, Qi LH, Chen GD (2006) New inverse method for identification of constitutive parameters. Trans Nonferrous Met Soc Chi 16:148–152
42. Anaraki MT, Sanjari M, Akbarzadeh A (2008) Modeling of high temperature rheological behavior of AZ61 Mg-alloy using inverse method and ANN. Mater Des 29:1701–1706
43. Zhang CS, Ding J, Dong YY, Zhao GG, Gao AJ, Wang LJ (2015) Identification of friction coefficients and strain-compensated Arrhenius-type constitutive model by two-step inverse analysis technique. Int J Mech Sci 98:195–204